

Monolithic multimodal neural probes for sustained stimulation and long-term neural recording

Luxi Zhang^{1,2,3}, Shengming Wang¹, Jie Xia^{1,2,3}, Boyu Li^{1,2,3}, Shaomin Zhang^{4*}, Jikui Luo¹, Fan Zhang⁴, Tianyu Zheng⁴, Gang Pan³, Tawfique Hasan⁵, Yanlan Yu⁶, Guoqing Ding⁶, Hao Jin^{1*}, Zongyin Yang^{1*}, Shurong Dong^{1,2,3*}

Long-term implantable neural probes with dual-mode optical stimulation and simultaneous electrical recording are crucial for modulating neural loop activity *in vivo*. Traditional probes using “add-on” strategies often suffer from mechanical rigidity, compromised electrical performance, and insufficient biocompatibility, limiting their clinical applicability. In this study, we present a method for the direct laser writing of electrode arrays onto the curved surface of optical fibers, integrating them within a biocompatible polymer coating to create monolithic neural probes. The monolithic probes demonstrate high mechanical bending endurance, stable impedance, and improved biocompatibility, resulting in a lower inflammatory response compared to conventional systems. Furthermore, our method facilitates the multilayer integration of multilayer electrodes onto optical fibers, enabling high-density electrical readout channels. This advancement represents substantial progress in neuroengineering, with promising implications for future neural monitoring and modulation applications.

INTRODUCTION

Optogenetic technology offers therapeutic pathways for neurological diseases like Parkinson’s disease, epilepsy, and chronic pain (1–3). By precisely targeting neural circuits, it alleviates motor dysfunctions in Parkinson’s disease (4–7), reduces seizures in epilepsy (8–11), and regulates pain pathways (12–14). These advances substantially affect neuroscience research, enhancing our understanding of neurological disorders and enabling more personalized, effective treatments. Neural probes with integrated neural optical stimulation during electrical recording are a basic tool in brain optogenetics (15–23). It combines electrical and optical functionalities to facilitate both the observation and regulation of neural loop activity *in vivo* (24–29). For example, optical fiber-integrated microelectrode arrays can perform neural optical stimulation while recording local neuroelectrical signals with microelectrode arrays to allow researchers to study complex dynamic processes in the brain. This multifunctionality not only helps our understanding of neural loop activities but also offers an effective method for neural modulation therapies for neurological disorders (30).

However, the integration of electrical components onto the curved and small surfaces of optical fibers is challenging. Current techniques for fabricating electrodes on the curved surface of optical fibers include inkjet printing (23, 31, 32), nanoimprinting (33), and water transfer printing (22). However, these “add-on” strategies involve sophisticated microfabrication techniques with low-yield and conductive materials that cannot adhere well to the optical fiber surface. This “add-on” approach also suffers from low mechanical

reliability for long-term accurate neural recording (31). A better and more robust scenario would be to fabricate electrodes inside the coating layer or the substrate of the optical fiber to create a monolithic neural probe.

In this work, we present an approach for developing monolithic fiber-based neural probes that seamlessly integrate optical stimulation and electrical recording capabilities. Our technology leverages a facile and scalable fabrication method to directly write electrode arrays onto the curved outer cladding of optical fibers using laser-assisted fabrication combined with a reducing agent. This eliminates the need for external wires or hybrid assembly techniques, which are often prone to mechanical failure and signal degradation over time.

The reducing agent facilitates efficient *in situ* reduction of gold nanoparticles (AuNPs) while minimizing damage to the polymer coating of the optical fiber. The resulting monolithic neural probe demonstrates a low starting impedance ($Z \approx 600$ ohms) and exceptional stability after 100 bending cycles. We implanted the probe in the brain of a mouse, simultaneously injecting viruses for *in vivo* brain signal measurements. The probe successfully records optogenetic signals under laser stimulation for up to 16 weeks, showing no significant signal deterioration, thus positioning it as a promising candidate for long-term implantable neural probes. In addition, our AuNP-fiber probe exhibits excellent biocompatibility, with notably reduced immunohistochemical responses compared to commercially available rigid probes. We also explore the optimization of electrode linewidth through varying laser pulse widths and enable the multilayer integration of multilayer electrodes onto optical fibers, facilitating high-density readout channels.

By combining the advantages of optical fibers—including minimal tissue damage, efficient light delivery, and compatibility with deep brain structures—with integrated microscale electrodes, our platform enables precise spatial and temporal control of neural circuits. The result is a versatile and scalable tool that bridges the gap between advanced optogenetic stimulation and high-fidelity electrophysiological monitoring, offering broad applicability in both basic and translational neuroscience research.

Copyright © 2025 The Authors, some rights reserved; exclusive licensee American Association for the Advancement of Science. No claim to original U.S. Government Works. Distributed under a Creative Commons Attribution NonCommercial License 4.0 (CC BY-NC).

¹College of Information Science and Electronic Engineering, Institute of Fundamental and Transdisciplinary Research, Zhejiang University, Hangzhou 310027, China. ²Nanhu Brain-computer Interface Institute, Hangzhou 310000, China. ³State Key Laboratory of Brain-Machine Intelligence, Zhejiang University, Hangzhou 310027, China. ⁴Key Laboratory of Biomedical Engineering of Ministry of Education, Qিশi Academy for Advanced Studies, Zhejiang University, Hangzhou 310027, China. ⁵Department of Engineering, University of Cambridge, Cambridge CB3 0FA, UK. ⁶Sir Run Run Shaw Hospital, School of Medicine, Zhejiang University, Hangzhou 310020, China.

*Corresponding author. Email: yangzongyin@zju.edu.cn (Z.Y.); dongshurong@zju.edu.cn (S.D.); shaomin@zju.edu.cn (S.Z.); hjin@zju.edu.cn (H.J.)

RESULTS

Fabrication of the AuNP probe

Figure 1A illustrates the schematic diagram of the AuNP-fiber probe, integrating an optogenetic fiber with an eight-channel AuNP electrode array embedded in a polymer matrix. The optical fiber's stimulation area is engineered to include randomly distributed artificial defects by heating the fiber tip, which slightly stretches it to create a tapered region. The taper allows light to be emitted not only from the tip but also from the sides of the fiber probe (fig. S1 and table S1), facilitating multipoint and multidirectional stimulation. A precursor mixture of SU-8 2000.5 and Jeffamine D-230 (commercially available polyetheramine) was cross-linked onto the fiber surface to create the polymer matrix. SU-8 was selected for this application, given that it is an ideal material for ensuring the durability and safety of implantable devices over extended periods, attributed to its robust mechanical strength, excellent biocompatibility, and high biostability (34–36). The fiber was then immersed in a solution of chloroauric acid dissolved in acetonitrile. The gold salt solution percolated into the polymer matrix, where the growth and distribution of AuNPs were controlled through electron transfer facilitated by the amino groups from Jeffamine D-230 (fig. S2).

While the reduction of AuNPs could occur at room temperature, it proceeded at a slower rate and could not form electrodes. To achieve precise control over the location and density of AuNPs within the polymer matrix, we developed a laser-assisted *in situ* reduction strategy. By adjusting the laser's power density and scanning rate (fig. S3) (34, 35, 37–39), we were able to accurately localize nanoparticle growth (37). Although chloroauric acid can be reduced by the heat generated from the laser, the formation of AuNPs occurs too slowly and requires high laser power, which can damage the polymer matrix (fig. S4). In addition, the laser fused and sintered the grown AuNPs, forming robust and conductive electrodes embedded within the polymer matrix. Details of the fabrication process are provided in Materials and Methods, and the complete process diagram is illustrated in fig. S5. To demonstrate that laser processing does not affect the fiber probe's performance, we compare the mean and variance of the fiber's output wavelength shifts and coupling efficiencies at four different light wavelengths (figs. S6 and S7) and report the fiber losses before and after metal deposition (table S2).

As illustrated in Fig. 1B, the probe features eight AuNP contact pads for extracellular electrical recording, along with corresponding AuNP microelectrodes for signal retrieval and connection to

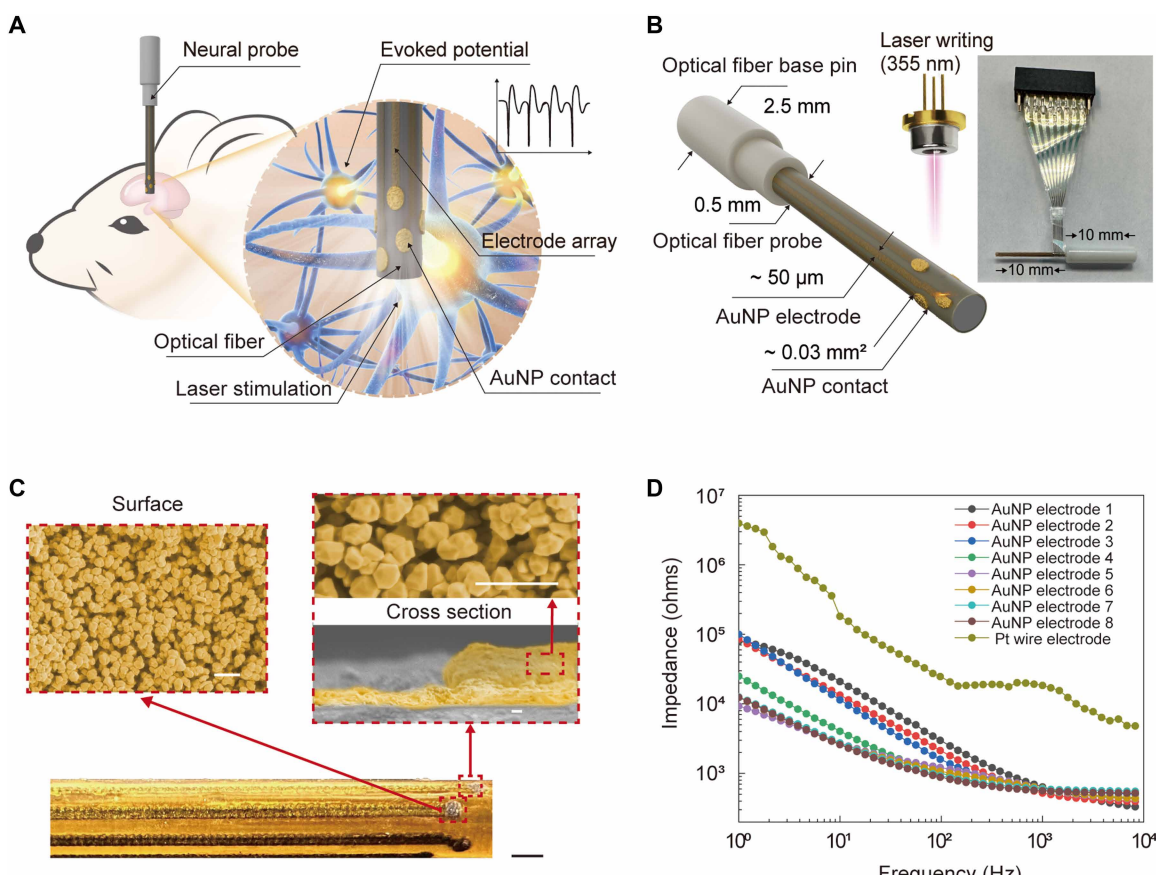


Fig. 1. AuNP-fiber probe. (A) Schematic of the fiber probe implanted into a mouse brain for laser stimulation and evoked electrical signal detection. (B) Illustration of the laser-based *in situ* reduction process used to fabricate the embedded AuNP electrodes. Inset: optical image of the AuNP-fiber probe with an FPC connector. (C) Microscopic image of the fabricated AuNP-fiber probe (scale bar, 200 μ m). Inset: SEM image (gold markers) of the Au nanoparticles and schematic of the embedded AuNP electrode (scale bars, 2 μ m). (D) Impedance spectra comparing an eight-channel AuNP-fiber probe with a Pt wire electrode.

electrophysiology monitoring equipment. To prevent the microelectrodes from recording unwanted electrical signals, a two-layer configuration is used. First, the microelectrodes are fabricated, followed by the application of another polymer layer. It is worth noting that the dimensions of the electrode array could be reduced for smaller laser irradiation areas. Contact pads are then formed on the surface by laser exposure, while the unexposed region is washed to create an insulating layer to prevent direct contact between the microelectrodes and tissue. An optical image of the complete AuNP-fiber probe integrated with the headstage connection system is shown in fig. S8. The surface and cross-sectional scanning electron microscopy (SEM) images of the fabricated probe are shown in Fig. 1C, where embedded AuNPs are pseudocolor enhanced for better visualization. SEM (without pseudocoloring) and energy-dispersive x-ray spectroscopy of the AuNP electrodes are presented in fig. S9, which demonstrate the fine-tuning of multilayer electrode formation and ensure strong integration of the AuNPs within the polymer structure.

We evaluated the electrochemical properties of our fiber probe (quasicircular with a diameter of ~100 μm) in comparison with a commercial platinum (Pt) wire electrode (exposed area of ~700 μm^2 ; Fulanke Technology Co., China). Both the AuNP-fiber probe and Pt wire electrode were immersed in a normal saline (NS) solution. Electrochemical impedance spectroscopy (EIS) performed across

the 1 Hz to 10 kHz range (Fig. 1D) showed that the impedance of our probe is two orders of magnitude lower than that of the Pt electrode, which we attribute to the larger active area and rough surface of the fused AuNP pads. Furthermore, the impedance across the eight-channel electrode array was consistent, ranging from 524.60 to 640.80 ohms at 1 kHz (SD: 33.97 ohms), demonstrating the reliability of our fabrication process (fig. S10).

In vitro characterization of the AuNP-fiber probe

We characterize the signal coherence of the eight microelectrodes of the AuNP-fiber probe by measuring signals while the probe is immersed in NS. An electrophysiological signal generator (CerePlex, Blackrock, US) is used to generate the signal, and the eight-channel electrode array concurrently records the corresponding signal. The eight microelectrodes show excellent consistency in both the frequency and shape of the measured signals (fig. S11). We compare the electrical performance of the AuNP electrode with that of the Pt wire electrode, along with the in vitro monitoring of electrophysiological signals over 2 min. The electrophysiological signal distribution of both electrodes is similar in the low-frequency range, which corresponds to the region where electroencephalography signals are found. It is clear that the electrophysiological signals obtained by the AuNP electrode have a higher amplitude, with an average signal amplitude 1.37 times that of the Pt wire electrode (Fig. 2A). This further

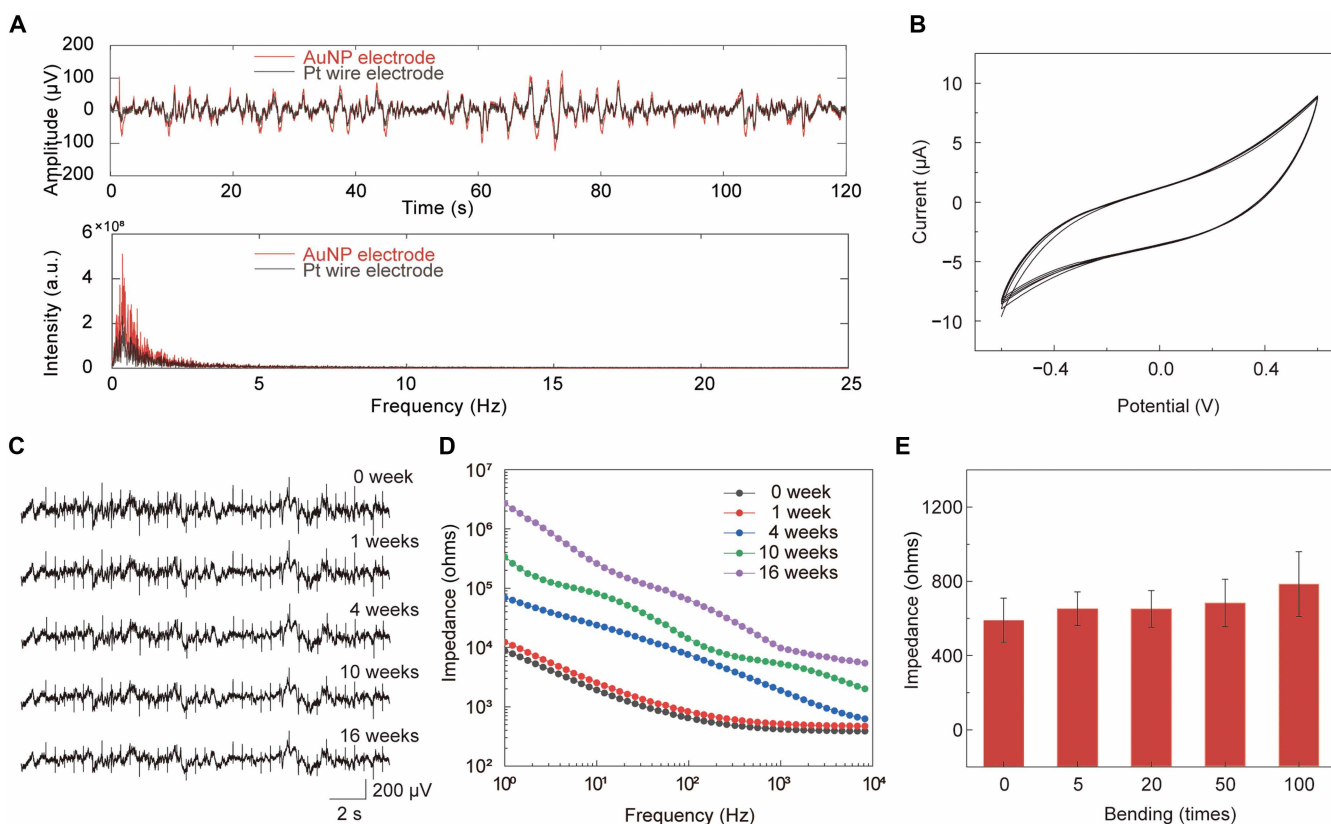


Fig. 2. In vitro characterization of the AuNP-fiber probe. (A) Performance comparison between the AuNP electrode and the commercial electrode (Pt wire). The upper panel shows the comparison of electrophysiological signals, and the low panel shows the comparison of power spectra of the two electrodes. a.u., arbitrary units. (B) CV curves of a single electrode from the eight-channel AuNP-fiber probe. (C) In vitro electrophysiological signals were measured simultaneously with individual AuNP electrodes infiltrated in NS for 0, 1, 4, 10, and 16 weeks. (D) Impedance spectra were measured with individual AuNP electrodes infiltrated in NS for 0, 1, 4, 10, and 16 weeks. (E) Impedance variation of a single AuNP electrode with cyclic bending, showing stable performance and consistent impedance values.

confirms that the impedance of the AuNP electrode is lower than that of the Pt wire electrode.

Stability is a crucial requirement for neural electrodes, and it can be evaluated using cyclic voltammetry (CV) measurements. CV measurements were performed on the AuNP electrode using an electrochemical workstation over 20 cycles, as shown in Fig. 2B. After multiple cycles, no significant redox peaks were observed, indicating that no residual unreduced gold ions remained on the surface of the AuNP-fiber probe during fabrication. This ensures the probe's nontoxicity to living tissues and confirms its stable charge transfer capability postimplantation.

As shown in Fig. 2C, we further evaluated the stability of the AuNP-fiber probes for electrophysiological signal measurement. Five probes were immersed in NS for 0 (unimmersed), 1, 4, 10, and 16 weeks. Electrophysiological signals were simultaneously collected by all five probes. Even after 16 weeks of immersion, the AuNP electrodes remained functional, with only a slight decrease in signal amplitude (15%) compared to unimmersed electrodes. The signal curves also remained highly consistent. In addition, we tracked weekly impedance variations (Fig. 2D and fig. S12). Results showed that impedance increased by only one order of magnitude following prolonged NS exposure, further confirming the electrical stability of the embedded AuNP electrodes. To evaluate the flexibility of the AuNP-fiber probe, we bent the probe at a 60° angle (1-cm arc, bending radius of ~0.96 cm) for 5, 20, 50, and 100 cycles. The impedance values at 1 kHz remained below 800 ohms even after 100 bending cycles, showing no significant changes (Fig. 2E). This demonstrates that the electrical properties of the AuNP-fiber probe were not affected by the bending (40). The impedance diagram in fig. S13 also confirms the high stability of the electrode array, which we attribute to the embedding of the

metal electrodes within the polymer on the fiber surface. In addition, during in vitro electrophysiological signal experiments, lasers of varying powers and wavelengths were coupled into the AuNP-fiber probe, with no noticeable change in the received signals. This indicates that the lasers did not interfere with the acquisition of electrophysiological signals in the carrier experiments (fig. S14).

Biocompatibility of the AuNP-fiber probe

Prolonged implantation of probes often results in the formation of glial scarring (41), which encases the probe and hinders its contact with surrounding tissues, compromising the acquisition of clear electrical signals (42). To ensure long-term stable recording of electrophysiological signals in living tissues, it is essential to suppress the immune response. To assess the biocompatibility of the AuNP-fiber probe, we implanted it in the left hemisphere of a mouse's brain, while a Pt wire electrode was implanted in the right hemisphere for the comparison of the biocompatibility between the two probes.

Immunohistochemistry analysis of brain slices from the implantation sites was performed at 4 and 10 weeks postimplantation. The sections were stained using ionized calcium-binding adaptor molecule 1 (Iba1) and glial fibrillary acidic protein (GFAP), markers for microglia and astrogliosis, respectively. Fluorescence microscopy images revealed lower expression of GFAP and Iba1 around the insertion sites of the AuNP-fiber probe compared to the Pt wire electrode at both 4 and 10 weeks after implantation (Fig. 3A). Quantitative analysis of Iba1 and GFAP expression (Fig. 3B), derived from measurements along the two white dashed lines, was used to compare the chronic immune response between the probes. The average immunoreactivity density around the AuNP-fiber probe was lower than that of the Pt electrode. In addition to comparing GFAP and Iba1

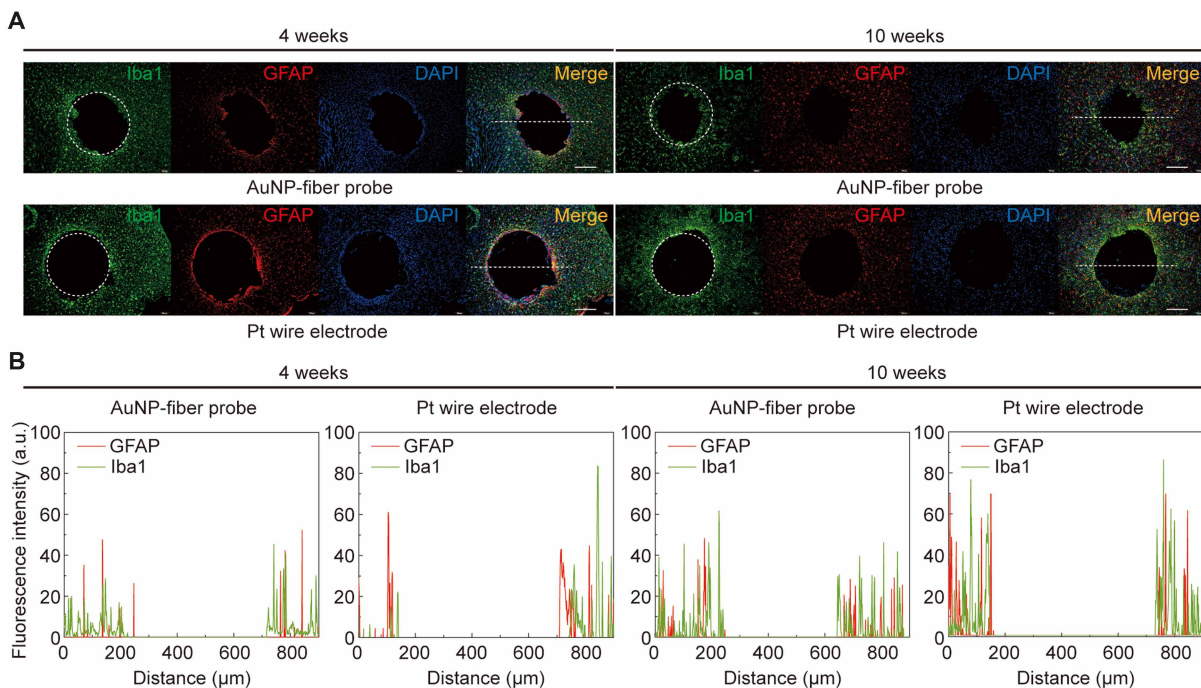


Fig. 3. Immunohistochemistry analysis. (A) Fluorescence microscopy images of DAPI (blue), GFAP (red), and Iba1 (green) after 4 and 10 weeks of implantation of both the AuNP-fiber probe and platinum wire electrode probe (scale bars, 200 μ m). (B) Quantitative fluorescence intensity of GFAP and Iba1 after 4 and 10 weeks of implantation of both the AuNP-fiber probe and platinum wire probe.

expression around the implanted probes, we also examined deeper implantation sites (fig. S15) and found that the AuNP-fiber probe exhibited lower immunoreactivity at these locations. This indicates that the AuNP-fiber probe induces a significantly lower immune response, enabling high-quality signal recording over long-term implantation. While the biosafety of the commercial Pt wire electrode is widely recognized by medical organizations (43–46) and confirmed by numerous studies (47, 48), our AuNP-fiber probe demonstrates even better biocompatibility. We attribute this to the probe's lower mechanical stiffness and greater flexibility compared to the Pt wire electrode, allowing it to better conform to the shape and movement of living tissue, causing less damage and irritation. This reduces the likelihood of tissue rejection or adverse reactions.

Optogenetics monitoring using the AuNP-fiber probe

Channelrhodopsin-2 (ChR2) is the most commonly used photosensitive protein for validating optogenetic devices (49, 50). Here, we use ChR2 to validate the ability of our fiber probe to simultaneously perform photostimulation and electrical signal monitoring in living tissue. To monitor the optogenetic signal, we injected the pAAV-hSyn-hChR2(H134R)-mCherry virus into the superior colliculus (SC) of a mouse brain while simultaneously implanting the AuNP-fiber probe in the same region. Robust ChR2 expression in the SC (51, 52) was observed 2 weeks after injection, whereas no such expression was detected in controls (not injected with ChR2) (fig. S16). The simultaneous recording of evoked electrical potentials from the eight microelectrodes in the SC, under 473-nm laser pulse stimulation, is shown in Fig. 4A over a 30-s period. Meanwhile, we calculated the SNR of each electrode on the AuNP fiber probe ($n = 3$) (shown in table S3). These results demonstrate that the implanted probe can stably record both spontaneous and evoked neural signals in the deep brain, with consistent results across all eight channels, indicating the good uniformity of the microelectrodes. Figure S17 presents the power spectrum of a single AuNP electrode under optical stimulation (5 mW, 1 Hz, 5 ms). Throughout 16 weeks, the recorded local field potential signals consistently remained within the low-frequency range, exhibiting no substantial spectral shifts and only a slight reduction in signal power over time. These results indicate the robust long-term stability of the electrode during chronic *in vivo* implantation.

We varied the incident laser pulse intensities, widths, and frequencies to assess the electroencephalography signal transmission capability of the AuNP-fiber probe. We analyzed the characteristics of spikes isolated from the recorded potentials within the 1 to 10 Hz frequency range (Fig. 4B). The results demonstrate that the evoked potential frequency aligns with the laser frequency, while the amplitude of the evoked potentials decreases as the laser frequency increases. When examining the mean amplitude of evoked potentials over time, the pattern was consistent with viral expression. The mean amplitude increased from week 2 to week 5, followed by a gradual decrease from week 5 to week 16 (Fig. 4C). Figure 4 (D and E) shows the variation in evoked potential signals with pulse widths ranging from 1 to 10 ms and laser powers between 5 and 15 mW. The average peak amplitude increased with longer pulse widths and higher laser power. Figures S18 to S20 provide comprehensive records of the amplitude trends of optogenetically evoked potentials from week 2 to week 16. In our experiment, the degree of ChR2 virus expression increased during the first week and then decreased in the subsequent week, which aligns with findings reported in the literature (21, 52).

Optimization for high-density readout channels

To enhance the spatial resolution of neural signals and increase the number of signal collection points and readout channels, we investigated the reduction of electrode size and the multilayer integration of an electrode array on our AuNP-fiber probe. While using a smaller focused laser beam could theoretically write thinner electrodes, the electrode width is significantly constrained by the thermal diffusion in the laser-heated zone. Figure 5A shows the simulated thermal distribution on the sample surface for a single femtosecond pulse (10 fs) and a single nanosecond pulse (10 ns). The portions of the curves above the blue dotted line indicate temperatures sufficient for AuNP growth and fusion into a continuous electrode (34). The data reveal that the heat from the shorter pulse width (10 fs) is more concentrated on the sample surface. The simulation results suggest that using a shorter pulse width (femtosecond) produces narrower and more well-defined AuNP electrode lines. To validate this, we conducted experiments using both a femtosecond laser (Fig. 5B) and nanosecond laser (Fig. 5C) on the same sample, keeping the spot size at 20 μm . The results show that the nanosecond laser-produced electrodes had wider linewidths and less defined edges because of more pronounced thermal diffusion. Thus, electrode width can be optimized by using a shorter pulse laser. Furthermore, a multilayer electrode array fabrication strategy was developed for multilayer integration on our AuNP-fiber probe. Figure 5D presents the schematic and SEM images of the multilayer electrodes, where the isolation layer was made from fully cross-linked SU-8 2000.5, and the cross-sectional dimensions of the electrodes were ~20 μm by 40 μm . The electrodes in each layer remained electrically isolated, confirming the feasibility of multilayer electrode probe fabrication. A detailed process description is provided in fig. S21.

DISCUSSION

We demonstrated that a laser-assisted fabrication method allows the direct writing of AuNP electrodes onto the curved surfaces of optical fibers, addressing the challenges of traditional “add-on” techniques. This approach not only enhances the mechanical reliability of the probe but also achieves low impedance, high flexibility, high stability, and excellent biocompatibility (table S4), as demonstrated by stable signal recording over 16 weeks of *in vivo* experiments. In addition, the ability to optimize the electrode linewidth and integrate multilayer electrodes further increases the spatial resolution and readout capabilities of the probe. This innovation holds great potential for both fundamental neuroscience research and therapeutic applications in neurological disorders, providing a robust tool for long-term neural modulation and signal acquisition.

MATERIALS AND METHODS

Materials

Chloroauric acid trihydrate ($\text{HAuCl}_4 \cdot 3\text{H}_2\text{O}$) was obtained from Aicon, China. Jeffamine D-230 was purchased from distributors of Macklin. Acetonitrile (anhydrous, 99.0%) was purchased from Sino-pharm Chemical Reagent Co., China. SU-8 2000.5 was obtained from Kayaku, Japan. For the precursor mixture, 10 g of SU-8 2000.5 and 50 mg of Jeffamine D-230 were mixed evenly in a 20-ml windowless glass bottle and then defoamed by a vacuum defoamer for 5 min. Separately, 0.394 g of chloroauric acid trihydrate was dissolved in 10 ml of acetonitrile, making 100×10^{-3} M chloroauric acid

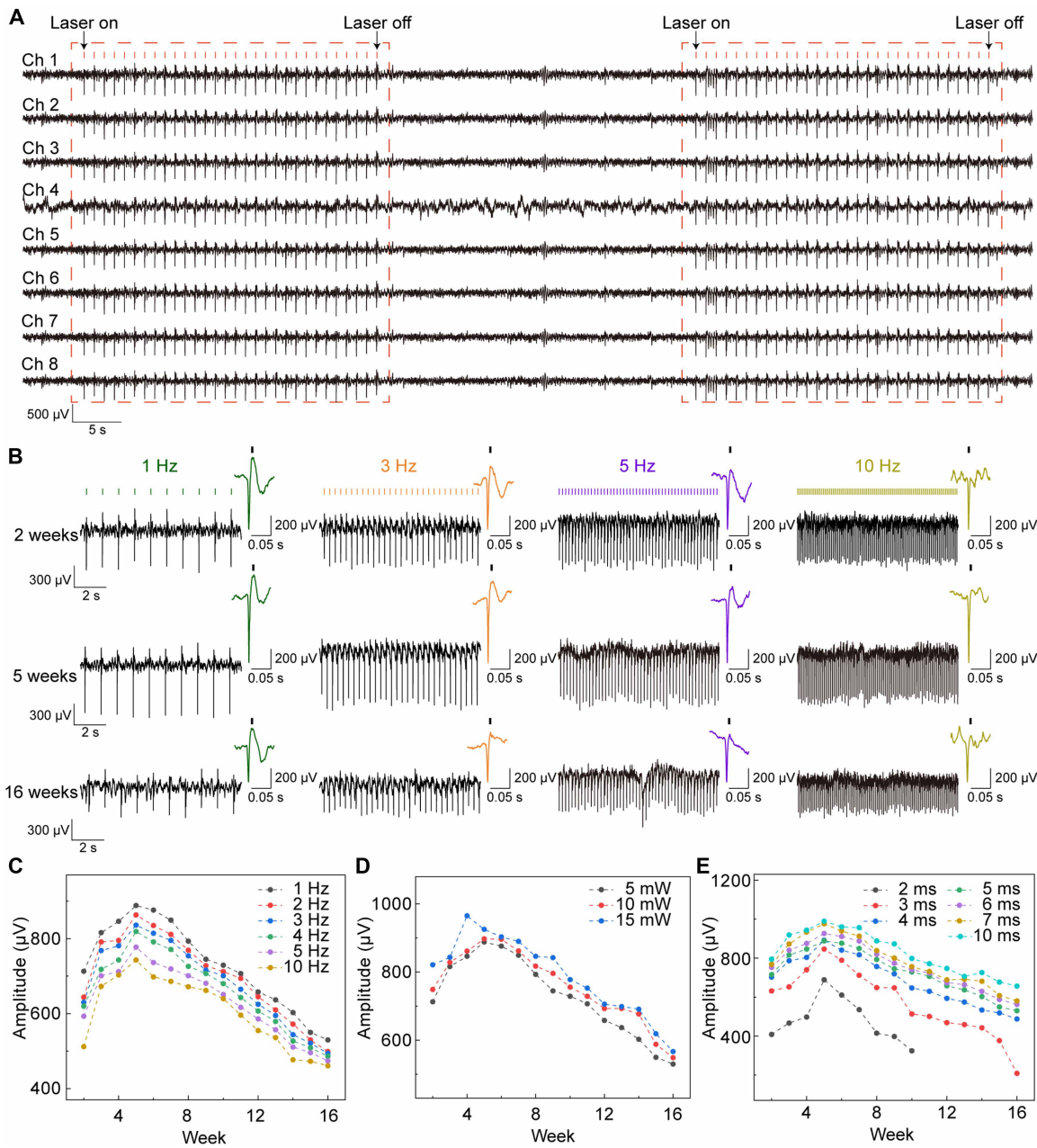


Fig. 4. In vivo electrophysiological recording using the AuNP-fiber probe. **(A)** The evoked potentials are recorded by eight microelectrodes of the fiber probe implanted in the SC region. **(B)** Simultaneous optogenetic stimulation (5-ms pulse width, 5-mW pulse intensity, and 1- to 10-Hz pulse frequency) and electrophysiological recordings are performed from 2 to 16 weeks after implantation. The upper right corner is a single evoked potential isolated from the recording. Amplitude variation of individual optogenetic signals recorded for 16 weeks **(C)** for different laser frequencies, **(D)** for different laser powers, and **(E)** for different laser pulse widths.

solution. The precursor mixture and chloroauric acid solution are refrigerated at 4°C.

Fabrication of the AuNP-fiber probe

Commercial optogenetic fibers (500 μ m in diameter; Xi'an Zhengkai Optoelectronics Technology Co., China) were used to fabricate the optical fiber probe with integrated AuNP electrodes. The precursor mixture (SU-8 2000.5 and Jeffamine D-230) was uniformly coated on the side surface of an optogenetic fiber using a mold. After baking at

95°C for 4 min, the coating was cross-linked via ultraviolet light. The solution of chloroauric acid (100×10^{-3} M) was infiltrated in the cross-linked polymer, and the solvent (acetonitrile) was left to evaporate for 4 hours. Then, a picosecond pulse laser (355 nm; Guangdong PulseX Laser Technology Co., China) was used to scan (5 mm/s) the fiber sample, inducing the chloroauric acid reduction to generate AuNPs and fuse them to form the electrode. The probe was washed with acetonitrile to rinse off any un-reduced chloroauric acid, and the probe side electrodes were annealed and sintered at 250°C for 10 min.

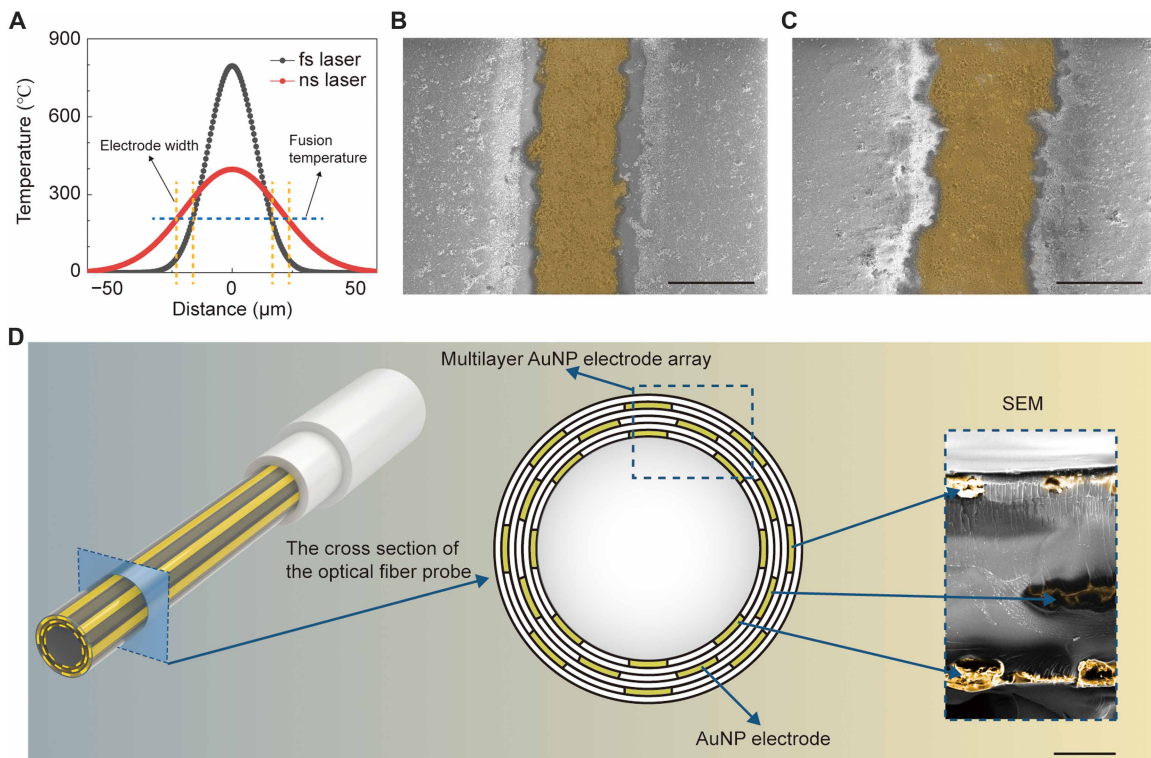


Fig. 5. Process optimization of the AuNP-fiber probe. (A) Average thermal distribution of a single femtosecond laser pulse and single nanosecond laser pulse. AuNP electrode (gold markers) prepared (B) by femtosecond (fs) laser pulses (scale bar, 50 μm) and (C) by nanosecond (ns) laser pulses (scale bar, 50 μm). (D) Schematic diagram and SEM (gold markers) of multilayer electrode arrays (scale bar, 50 μm).

Next, we developed a custom flexible printed circuit (FPC) connector to establish robust electrical connectivity between the probe electrodes and external circuitry. The FPC was designed with eight exposed electrode pads, each precisely aligned with the eight recording sites on the probe. To prevent direct tissue contact, these pads were insulated with a protective layer. The exposed FPC ends were coated with anisotropic conductive adhesive, enabling reliable electrical connections when rolled onto the probe surface. Subsequently, the SU-8 photoresist was applied to the outer connection area, serving as a biocompatible encapsulation while providing mechanical compliance that matches cortical tissue properties. Subsequently, a second layer of precursor mixture was coated on the side electrode of the fiber and baked at 95°C for 4 min. We followed the same procedure above to create the sintered AuNP contacts. Thus, the electrode array and edge of the contacts were embedded in the cross-linked polymer, with only the contacts exposed for recording neural signals (shown in Fig. 1B).

The fiber probe was optically characterized by a three-dimensional microscope (homebuilt equipment). The microstructure of the probe was assessed by SEM (Auriga 40, Zeiss, Germany).

In vitro characterization of optical properties

Pulsed lasers with 480-, 532-, 570-, and 632-nm wavelengths from Wuhan Yangtze Soton Laser Co., Ltd. (China), were used for the experiments. To determine the optical transmission loss before and after laser processing, laser beams with different wavelengths were selected as the incident light source and were coupled into the fiber. The output optical power before and after etching (five AuNP-fiber probes were used) was evaluated separately using an optical power

meter (Thorlabs, PM100USB, 350 to 1100 nm, US). Transmission spectral analysis was conducted with a spectrometer from Ocean Optics (USB4000, 345 to 1041 nm, UK) for wavelength calibration and the measurement of the wavelength shift before and after laser writing.

In vitro characterization of electrical properties

Conductivity measurement was performed using an LCR digital bridge (TH2832). To assess the electrical properties of the AuNP electrode array, the CV and Electrochemical Impedance Spectroscopy (EIS) images of the AuNP electrodes (five AuNP-fiber probes were used) were obtained by an electrochemical workstation (CHI760E, CH Instrument Co., Ltd., US), adopting a three-electrode configuration in NS. The integrated probe, Ag/AgCl, and graphite (Shanghai Fan Yue Electronic Technology Co., Ltd., China) were used as the working electrode, reference electrode, and counter electrode, respectively. The AuNP electrodes were measured for 20 cycles of CV (0.1 V/s, -0.6 to 0.6 V) under the NS condition. Measurements of EIS with a sinusoidal input (5 mV, 1 Hz to 10 kHz) were performed. To prove the flexibility and stability of the electrodes, the electrodes (five AuNP-fiber probes were used) were bent 5, 20, 50, and 100 times and then recovered to measure the EIS. The physiological electrical signal sensing capability of AuNP electrodes was characterized by an electrophysiological signal generator purchased from CerePlex (Blackrock, US), which could generate a simulated signal of local field potential and spikes in the NS solution. Electrode impedance was measured using a CerePlex μ16 headstage (Blackrock Neurotech). The system delivers a 1-kHz, 1-nA peak-to-peak current pulse (100-ms duration) to each electrode. Measurements

between 1 kilohm and 2 megohms were considered valid; values below 100 kilohms indicated stable connections and functional recording channels.

Surgery and virus injection

The AuNP-fiber probe was verified in male adult C57BL mice (25 g). All the animals and experimental procedures were carried out in accordance with the Guide for the Care and Use of Laboratory Animals (China Ministry of Health) and were approved by the Animal Care Committee of Zhejiang University, China (approval no. ZJU20200130).

1) Preoperative preparation: Animals were fully acclimatized for 7 days and were given standard rat chow and water. The mice were anesthetized by isoflurane, and the head was fixed to the stereotaxic apparatus (RWD, China).

2) Surgical procedure: Head skin was incised to expose the skull with the appropriate content of hydrogen peroxide and saline scrub. Then, a tiny craniotomy hole was made using a dental drill (RWD, China) for virus injection and probe implantation. Virus serotype 9 (adeno-associated virus 2) carrying pAAV-hSyn-hChR2(H134R)-mCherry was purchased from OBiO Technology (Shanghai) Corp., Ltd. The virus (0.2 ml) was injected into the SC [AP (anteroposterior): −3.7 mm; ML (mediolateral): −0.55 mm; DV (dorsoventral): −1.35 mm] with a glass microinjector (BF150-86-10, Sutter Instrument Co., China). Then, AuNP-fiber probes were implanted into the SC region of mice ($n = 3$).

3) Postoperative management: Probes were firmly mounted with dental cement, with a subcutaneous injection of ceftriaxone sodium (Sinopharm Chemical Reagent Co., China) for anti-inflammatory purposes. Mice recovered under standard housing conditions with free access to food/water.

In vivo neural signal recording

Active mice were placed in a transparent box; laser stimulation with different pulse widths, frequencies, and powers was applied to the brain; and the evoked potential was measured using a recording system. A blue laser with a 473-nm wavelength (Shanghai Laser & Optics Century Co., Ltd., China) was used. We perform laser (473 nm) power calibration before each optical stimulation experiment to ensure that the total power values at 1 mm from the fiber tip are 5, 10, and 15 mW, and the corresponding power densities are 1.59, 3.18, and 4.78 mW/mm², respectively. The side laser power densities near the tip average about 1.27, 2.54, and 3.82 mW/mm². Each light pulse train was triggered by an electrical stimulator (Master-8, A.M.P.I Instruments Ltd., Israel) with a pulse width varied from 1 to 10 ms, a pulse frequency from 1 to 10 Hz, and an excitation power of 5, 10, and 15 mW. Neural activity in the mouse SC was recorded at weekly intervals using a CerePlex signal processing system. Before each recording, electrode impedance was measured by the CerePlex μ 16 headstage. In impedance mode, the CerePlex μ delivers a 1-kHz, 1-nA peak-to-peak current pulse (100-ms duration) to each electrode. The system maintains the measurement accuracy within 1 kilohm to 2 megohms, and values below 100 kilohms indicate reliable device connections and confirm that the electrode channels are functioning properly. After impedance evaluation, neural activity was continuously recorded (2000 samples/s), with intermittent optogenetic stimulation applied midway using varying laser parameters. During the optogenetic stimulation block, a square wave with programmable parameters was delivered via PulsePal to serve as an external trigger for the laser. All the recordings were obtained in the unipolar

mode at a sampling frequency of 2 kHz, unless specified otherwise, and filtered with a high-pass filter of 0.2 Hz (four orders, Butterworth) in MATLAB (MathWorks).

Immunohistochemistry analysis

To evaluate the long-term stability and biocompatibility of the AuNP-fiber probe, a histological analysis of the brain for about 4 and 10 weeks was conducted. The AuNP-fiber probe and commercial electrodes (platinum wire, 500 μm in diameter) were implanted into the SC (AP: −3.7 mm; ML: −0.55 mm; DV: −1.35 mm) in the left and right brain, respectively (three mice were used for the 4- and 10-week experiments, respectively). After 4 and 10 weeks, the male mice were perfused transcardially with cold physiological saline, the AuNP-fiber probe and commercial electrode (Pt) were removed, and then the brain tissue was immersed in 4% formaldehyde and fixed in centrifuge tubes (50 ml). After 48-hour fixation, the brain tissue was dehydrated, embedded, and then sliced horizontally into 3-μm-thick slices. The slices were stained with an antibody in 0.1 M PBS containing 3% (w/v) bovine serum albumin: anti-GFAP (1:200, Abcam, ab207165), anti-Iba1 (1:2000, Abcam, ab178846), and anti-DAPI (4',6-diamidino-2-phenylindole) (1:1, Merck, 28718-90-3). After primary staining, the primary antibody-conjugated brain slices were incubated with a secondary antibody: anti-GFAP (1:100, Okoya, Opel520), anti-Iba1 (1:100, Okoya, Opel570), and anti-DAPI (1:1, Merck, 28718-90-3). The slices were examined under epifluorescence using a microscope. The brain slices were imaged using a confocal microscope and analyzed using Zeiss Zen software (LSM 700, Carl Zeiss, Oberkochen, Germany). In addition, the fluorescence intensity of the line plot profile was analyzed using ImageJ.

Supplementary Materials

The PDF file includes:

Figs. S1 to S21

Tables S1 to S4

Legend for movie S1

Other Supplementary Material for this manuscript includes the following:

Movie S1

REFERENCES AND NOTES

1. A. M. Packer, B. Roska, M. Häusser, Targeting neurons and photons for optogenetics. *Nat. Neurosci.* **16**, 805–815 (2013).
2. O. A. Shemesh, D. Tanese, V. Zampini, C. Linghu, K. Piatkevich, E. Ronzitti, E. Papagiakoumou, E. S. Boyden, V. Emiliani, Temporally precise single-cell-resolution optogenetics. *Nat. Neurosci.* **20**, 1796–1806 (2017).
3. S. A. Josselyn, The past, present and future of light-gated ion channels and optogenetics. *eLife* **7**, e42367 (2018).
4. D. M. Wilson III, M. R. Cookson, L. Van Den Bosch, H. Zetterberg, D. M. Holtzman, I. Dewachter, Hallmarks of neurodegenerative diseases. *Cell* **186**, 693–714 (2023).
5. P. Barroso-Chinea, M.-L. Thioliat, S. Bido, A. Martinez, E. Doudnikoff, J. Baufreton, M. Bourdenx, B. Bloch, E. Bezard, M.-L. Martin-Negrier, D1 dopamine receptor stimulation impairs striatal proteasome activity in Parkinsonism through 26S proteasome disassembly. *Neurobiol. Dis.* **78**, 77–87 (2015).
6. L. F. Hernández, I. Castela, I. R.-D. Diego, J. A. Obeso, R. Moratalla, Striatal activation by optogenetics induces dyskinesias in the 6-hydroxydopamine rat model of Parkinson disease. *Mov. Disord.* **32**, 530–537 (2017).
7. T. Bordia, X. A. Perez, J. E. Heiss, D. Zhang, M. Quik, Optogenetic activation of striatal cholinergic interneurons regulates L-dopa-induced dyskinesias. *Neurobiol. Dis.* **91**, 47–58 (2016).
8. M. C. Walker, D. M. Kullmann, Optogenetic and chemogenetic therapies for epilepsy. *Neuropharmacology* **168**, 107751 (2020).
9. J. Tønnesen, M. Kokaila, Epilepsy and optogenetics: Can seizures be controlled by light? *Clin. Sci.* **131**, 1605–1616 (2017).

10. M. Choy, B. A. Duffy, J. H. Lee, Optogenetic study of networks in epilepsy. *J. Neurosci. Res.* **95**, 2325–2335 (2017).
11. Y. Shimoda, K. Beppu, Y. Ikoma, Y. M. Morizawa, S. Zuguchi, U. Hino, R. Yano, Y. Sugiura, S. Moritoh, Y. Fukazawa, M. Suematsu, H. Mushiake, N. Nakasato, M. Iwasaki, K. F. Tanaka, T. Tominaga, K. Matsui, Optogenetic stimulus-triggered acquisition of seizure resistance. *Neurobiol. Dis.* **163**, 105602 (2022).
12. F. Guo, Y. Du, F.-H. Qu, S.-D. Lin, Z. Chen, S.-H. Zhang, Dissecting the neural circuitry for pain modulation and chronic pain: Insights from optogenetics. *Neurosci. Bull.* **38**, 440–452 (2022).
13. H. C. Moon, Y. S. Park, Optogenetic stimulation of the anterior cingulate cortex modulates the pain processing in neuropathic pain: A review. *J. Mol. Neurosci.* **72**, 1–8 (2022).
14. F. Iseppon, M. Arcangeletti, Optogenetics and photopharmacology in pain research and therapeutics. *STEMedicine* **1**, e43 (2020).
15. S. Park, H. Yuk, R. Zhao, Y. S. Yim, E. W. Woldegebriel, J. Kang, A. Canales, Y. Fink, G. B. Choi, X. Zhao, P. Anikeeva, Adaptive and multifunctional hydrogel hybrid probes for long-term sensing and modulation of neural activity. *Nat. Commun.* **12**, 3435 (2021).
16. W. Yan, I. Richard, G. Kurtuldu, N. D. James, G. Schiavone, J. W. Squair, T. Nguyen-Dang, T. Das Gupta, Y. Qu, J. D. Cao, R. Ignatans, S. P. Lacour, V. Tileli, G. Courtine, J. F. Loffler, F. Sorin, Structured nanoscale metallic glass fibres with extreme aspect ratios. *Nat. Nanotechnol.* **15**, 875–882 (2020).
17. B. Spagnolo, A. Balena, R. T. Peixoto, M. Pisanello, L. Sileo, M. Bianco, A. Rizzo, F. Pisano, A. Qualtieri, D. D. Lofrumento, F. De Nuccio, J. A. Assad, B. L. Sabatini, M. De Vittorio, F. Pisanello, Tapered fiberfrodes for optoelectrical neural interfacing in small brain volumes with reduced artefacts. *Nat. Mater.* **21**, 826–835 (2022).
18. M. Voroslakos, K. Kim, N. Slager, E. Ko, S. Oh, S. S. Parizi, B. Hendrix, J. P. Seymour, K. D. Wise, G. Buzsaki, A. Fernandez-Ruiz, E. Yoon, HectoSTAR muLED optoelectrodes for large-scale, high-precision *in vivo* opto-electrophysiology. *Adv. Sci.* **9**, e2105414 (2022).
19. L. Wang, C. Zhong, D. Ke, F. Ye, J. Tu, L. Wang, Y. Lu, Ultrasoft and highly stretchable hydrogel optical fibers for *in vivo* optogenetic modulations. *Adv Opt Mater* **6**, 1800427 (2018).
20. S. Jiang, D. C. Patel, J. Kim, S. Yang, W. A. Mills III, Y. Zhang, K. Wang, Z. Feng, S. Vijayan, W. Cai, A. Wang, Y. Guo, I. F. Kimbrough, H. Sontheimer, X. Jia, Spatially expandable fiber-based probes as a multifunctional deep brain interface. *Nat. Commun.* **11**, 6115 (2020).
21. C. Won, U. J. Jeong, S. Lee, M. Lee, C. Kwon, S. Cho, K. Yoon, S. Lee, D. Chun, I. J. Cho, T. Lee, Mechanically tissue-like and highly conductive Au nanoparticles embedded elastomeric fiber electrodes of brain-machine interfaces for chronic *in vivo* brain neural recording. *Adv. Funct. Mater.* **32**, 2205145 (2022).
22. J. Yu, W. Ling, Y. Li, N. Ma, Z. Wu, R. Liang, H. Pan, W. Liu, B. Fu, K. Wang, C. Li, H. Wang, H. Peng, B. Ning, J. Yang, X. Huang, A multichannel flexible optoelectronic fiber device for distributed implantable neurological stimulation and monitoring. *Small* **17**, e2005925 (2021).
23. M. S. Saleh, S. M. Ritchie, M. A. Nicholas, H. L. Gordon, C. Hu, S. Jahan, B. Yuan, R. Bezbarua, J. W. Reddy, Z. Ahmed, M. Chamanzar, E. A. Yttri, R. P. Panat, CMU Array: A 3D nanoprinted, fully customizable high-density microelectrode array platform. *Sci. Adv.* **8**, eabj4853 (2022).
24. V. Gradinariu, M. Mogri, K. R. Thompson, J. M. Henderson, K. Deisseroth, Optical deconstruction of parkinsonian neural circuitry. *Science* **324**, 354–359 (2009).
25. K. M. Tye, K. Deisseroth, Optogenetic investigation of neural circuits underlying brain disease in animal models. *Nat. Rev. Neurosci.* **13**, 251–266 (2012).
26. K. Deisseroth, Optogenetics. *Nat. Methods* **8**, 26–29 (2011).
27. B. Camporeze, B. A. Manica, G. A. Bonafé, J. J. C. Ferreira, A. L. Diniz, C. T. P. de Oliveira, L. R. M. Junior, P. H. P. de Aguiar, M. M. Ortega, Optogenetics: The new molecular approach to control functions of neural cells in epilepsy, depression and tumors of the central nervous system. *Am. J. Cancer Res.* **8**, 1900–1918 (2018).
28. L. Grosenick, J. H. Marshel, K. Deisseroth, Closed-loop and activity-guided optogenetic control. *Neuron* **86**, 106–139 (2015).
29. E. Segev, J. Reimer, L. C. Moreaux, T. M. Fowler, D. Chi, W. D. Sacher, M. Lo, K. Deisseroth, A. S. Tolias, A. Faraon, M. L. Roukes, Patterned photostimulation via visible-wavelength photonic probes for deep brain optogenetics. *Neurophotonics* **4**, 011002 (2017).
30. K. Deisseroth, Controlling the brain with light. *Sci. Am.* **303**, 48–55 (2010).
31. D. Afanasenkov, D. Kalinina, V. Lyakhovetskii, C. Tondera, O. Gorsky, S. Moosavi, N. Pavlova, N. Merkul'yeva, A. V. Kalueff, I. R. Minev, P. Musienko, Rapid prototyping of soft bioelectronic implants for use as neuromuscular interfaces. *Nat. Biomed. Eng.* **4**, 1010–1022 (2020).
32. W. Wang, K. Ouoras, A. L. Rutz, X. Li, M. Gerigk, T. E. Naegele, G. G. Malliaras, Y. Y. S. Huang, Inflight fiber printing toward array and 3D optoelectronic and sensing architectures. *Sci. Adv.* **6**, eaba0931 (2020).
33. B. Osmani, H. Schiff, K. Vogelsang, R. Guzman, P. M. Kristiansen, R. Crockett, A. Chacko, S. Bucher, T. Töpper, B. J. M. Müller, N. Engineering, Hierarchically structured polydimethylsiloxane films for ultra-soft neural interfaces. *Micro Nano Eng.* **7**, 100051 (2020).
34. E. K. W. Tan, P. K. Shrestha, A. V. Pansare, S. Chakrabarti, S. Li, D. Chu, C. R. Lowe, A. A. Nagarkar, Density modulation of embedded nanoparticles via spatial, temporal, and chemical control elements. *Adv. Mater.* **31**, e1901802 (2019).
35. A. V. Pansare, S. R. Khairkar, A. A. Hedge, S. Y. Chhatre, V. R. Patil, A. A. Nagarkar, In situ nanoparticle embedding for authentication of epoxy composites. *Adv. Mater.* **30**, e1801523 (2018).
36. Z. Chen, J.-B. Lee, Biocompatibility of SU-8 and its biomedical device applications. *Micromachines* **12**, 794 (2021).
37. S. Shukla, X. Vidal, E. P. Furlani, M. T. Swihart, K.-T. Kim, Y.-K. Yoon, A. Urbas, P. N. Prasad, Subwavelength direct laser patterning of conductive gold nanostructures by simultaneous photopolymerization and photoreduction. *ACS Nano* **5**, 1947–1957 (2011).
38. M. J. Tommalieh, H. A. Ibrahim, N. S. Awwad, A. A. Menaze, Gold nanoparticles doped Polyvinyl Alcohol Chitosan blend via laser ablation for electrical conductivity enhancement. *J. Mol. Struct.* **1221**, 128814 (2020).
39. Y. T. Cheng, R. H. Uang, Y. M. Wang, K. C. Chiou, T. M. Lee, Laser annealing of gold nanoparticles thin film using photothermal effect. *Microelectron. Eng.* **86**, 865–867 (2009).
40. B. Wester, R. Lee, M. C. LaPlaca, Development and characterization of *in vivo* flexible electrodes compatible with large tissue displacements. *J. Neural Eng.* **6**, 024002 (2009).
41. J. W. Salatino, K. A. Ludwig, T. D. Kozai, E. K. Purcell, Glial responses to implanted electrodes in the brain. *Nat. Biomed. Eng.* **1**, 862–877 (2017).
42. L. Luan, X. Wei, Z. Zhao, J. J. Siegel, O. Potnis, C. A. Tuppen, S. Lin, S. Kazmi, R. A. Fowler, S. Holloway, A. K. Dunn, R. A. Chitwood, C. Xie, Ultraflexible nanoelectronic probes form reliable, glial scar-free neural integration. *Sci. Adv.* **3**, e1601966 (2017).
43. L. Bareket, A. Barriga-Rivera, M. P. Zapf, N. H. Lovell, G. J. Suaning, Progress in artificial vision through suprachoroidal retinal implants. *J. Neural Eng.* **14**, 045002 (2017).
44. C. Boehler, D. M. Vieira, U. Egert, M. Asplund, Asplund, interfaces, NanoPt—A nanostructured electrode coating for neural recording and microstimulation. *ACS Appl. Mater. Interfaces* **12**, 14855–14865 (2020).
45. A. N. Dalrymple, M. Huynh, B. A. Nayagam, C. D. Lee, G. R. Weiland, A. Petrossians, J. John, J. B. Fallon, R. K. Shepherd, Electrochemical and biological characterization of thin-film platinum-iridium alloy electrode coatings: a chronic *in vivo* study. *J. Neural Eng.* **17**, 036012 (2020).
46. X. Zhang, C. Chen, G. Ni, Y. Hai, B. Chen, Y. Zhou, B. Zhang, G. Chen, M. M.-C. Cheng, Carbon multi-electrode arrays as peripheral nerve interface for neural recording and nerve stimulation. *Med. Devices Sens.* **2**, e10026 (2019).
47. M. A. Freire, E. Morya, J. Faber, J. R. Santos, J. S. Guimaraes, N. A. Lemos, K. Sameshima, A. Pereira, S. Ribeiro, M. A. Nicolelis, Comprehensive analysis of tissue preservation and recording quality from chronic multielectrode implants. *PLOS ONE* **6**, e27554 (2011).
48. C. A. Cordeiro, A. Sias, T. Koster, B. H. C. Westerink, T. I. F. H. Cremers, In *vivo* “real-time” monitoring of glucose in the brain with an amperometric enzyme-based biosensor based on gold coated tungsten (W-Au) microelectrodes. *Sens. Actuators B* **263**, 605–613 (2018).
49. L. A. Gunaydin, O. Yizhar, A. Berndt, V. S. Sohal, K. Deisseroth, P. Hegemann, Ultrafast optogenetic control. *Nat. Neurosci.* **13**, 387–392 (2010).
50. A. Dawydow, R. Gueta, D. Ljaschenko, S. Ullrich, M. Hermann, N. Ehmann, S. Gao, A. Fiala, T. Langenhan, G. Nagel, R. J. Kittel, Channelrhodopsin-2-XXL, a powerful optogenetic tool for low-light applications. *Proc. Natl. Acad. Sci. U.S.A.* **111**, 13972–13977 (2014).
51. Y. Dai, M. Du, L. Huang, J. Zheng, L. Wei, J. Qiu, C. Ren, S. Zhou, Multimaterial glass fiber probe for deep neural stimulation and detection. *Adv Opt Mater* **11**, 2202184 (2022).
52. M. Du, L. Huang, J. Zheng, Y. Xi, Y. Dai, W. Zhang, W. Yan, G. Tao, J. Qiu, K. F. So, C. Ren, S. Zhou, Flexible fiber probe for efficient neural stimulation and detection. *Adv. Sci.* **7**, 2001410 (2020).

Acknowledgments

Funding: This work was supported by the following: ST12030 major project (no. 2021ZD0200401), National Natural Science Foundation of China (no. 62334001), Science Challenge Project, Zhejiang Province Key R&D programs (nos. 2024C03001, 2021C03003, and 2024C03007), Zhejiang Province high level talent special support plan (no. 2022R52042), China Postdoctoral Science Foundation Funded Project (no. 2024M752790), and The Postdoctoral Fellowship Program of CPSF under grant (no. GZC20241457). **Author contributions:** Conceived the experiments: L.Z., S.W., H.J., S.D., and Z.Y. Designed the experiments: S.D., Z.Y., J.X., and S.Z. Process preparation: L.Z., S.W., and J.X. Testing: L.Z., S.W., J.X., B.L., and T.Z. Verification test: L.Z., F.Z., Y.Y., and G.D. Data processing and analysis: L.Z., G.P., T.H., and G.D. Writing—original draft: L.Z., S.W., S.D., and Z.Y. Writing—review and editing: S.D., Z.Y., J.L., and T.H. **Competing interests:** The authors declare that they have no competing interests. **Data and materials availability:** All data needed to evaluate the conclusions in the paper are present in the paper and/or the Supplementary Materials.

Submitted 28 October 2024

Accepted 25 August 2025

Published 26 September 2025

10.1126/sciadv.adu1753